Non-Abelian Topological Bound States in the Continuum

Long Qian,[1,*] Weixuan Zhang,[1,*,†] Houjuan Sun,[2] and Xiangdong Zhang[1,‡]

[1]Key Laboratory of advanced optoelectronic quantum architecture and measurements of Ministry of Education, Beijing Key Laboratory of Nanophotonics & Ultrafine Optoelectronic Systems, School of Physics, Beijing Institute of Technology, Beijing 100081, China

[2]Beijing Key Laboratory of Millimeter wave and Terahertz Techniques, School of Information and Electronics, Beijing Institute of Technology, Beijing 100081, China

(Received 30 June 2023; accepted 3 January 2024; published 22 January 2024)

Bound states in the continuum (BICs), which are spatially localized states with energies lying in the continuum of extended modes, have been widely investigated in both quantum and classical systems. Recently, the combination of topological band theory with BICs has led to the creation of topological BICs that exhibit extraordinary robustness against disorder. However, the previously proposed topological BICs are only limited in systems with Abelian gauge fields. Whether non-Abelian gauge fields can induce topological BICs and how to experimentally explore these phenomena remains unresolved. Here, we report the theoretical and experimental realization of non-Abelian topological BICs, which are generated by the interplay between two inseparable pseudospins and can coexist in each pseudospin subspace. This unique characteristic necessitates non-Abelian couplings that lack any Abelian counterparts. Furthermore, the non-Abelian couplings can also offer a new avenue for constructing topological subspace-induced BICs at bulk dislocations. Those exotic phenomena are observed by non-Abelian topolectrical circuits. Our results establish the connection between topological BICs and non-Abelian gauge fields, and serve as the catalyst for future investigations on non-Abelian topological BICs across different platforms.

DOI: 10.1103/PhysRevLett.132.046601

In 1929, von Neumann and Wigner proposed the concept of BICs, which are perfectly localized states coexisting with extended eigenmodes [1]. Recently, it has been recognized that BICs arise from wave interference phenomena. Consequently, extensive experimental verifications have been conducted to explore BICs in various classical wave systems [2–8]. Notably, BICs always exhibit enhanced resonances with ultrahigh Q factors, making them crucial for designing highly efficient devices [9–22]. More recently, the combination of topological band theory and BICs has led to the emergence of topological BICs [23–30], where eigenenergies of topological states are embedded within bulk bands without any hybridization. Topological BICs possess extraordinary robustness against disorder and significantly enhance wave manipulation capabilities. To date, investigations on topological BICs have been limited to systems with Abelian gauge fields.

In 1954, Yang and Mills proposed non-Abelian gauge fields [31]. Recently, the concept of non-Abelian synthetic gauge fields has been extended to real space and parameter spaces, revealing a plethora of novel phenomena with non-Abelian characteristics [32–44]. For instance, topological phases in multiple-band systems can be characterized using non-Abelian topological charges [34,35]. Non-Abelian braiding has been experimentally demonstrated in photonic and acoustic structures [36,37]. Furthermore, the Hofstadter model incorporating non-Abelian synthetic gauge fields [43] and the construction of non-Abelian Chern insulators [44] have showcased exotic physics arising from the interplay between these gauge fields and topological matters. Given recent advancements in both non-Abelian synthetic gauge fields and topological BICs, it is imperative to explore whether their intersection yields new physics.

In this work, we present the realization of non-Abelian topological BICs, and reveal the coexistence of pseudospin-selected non-Abelian BICs in each single pseudospin subspace. The non-Abelian topological BICs are observed by topolectrical circuits. Our results extend topological BICs into the non-Abelian region, and possess potential applications in robust electronic devices with non-Abelian features.

The theory of non-Abelian topological BICs.—We consider a two-dimensional (2D) lattice model in the presence of U(2) non-Abelian coupling matrices, as shown in Fig. 1(a). There are four sublattices marked 'a', 'b', 'c' and 'd' in a single unit. Each sublattice contains two internal pseudospins $|\uparrow\rangle_{a,b,c,d} = [1,0]^T$ and $|\downarrow\rangle_{a,b,c,d} = [0,1]^T$. The intracell (intercell) coupling matrices are in the form of $t_1\boldsymbol{\sigma}_z$ and $it_1\boldsymbol{\sigma}_y$ ($t_2\boldsymbol{\sigma}_z$ and $-it_2\boldsymbol{\sigma}_y$), as plotted by black (gray) solid and dashed arrows. Here, $\boldsymbol{\sigma}_z$ and $\boldsymbol{\sigma}_y$ are Pauli matrices. t_1 and t_2 represent intracell and intercell coupling strengths. Non-Abelian gauge fields require that at least two hopping matrices obeying the noncommutative relationship, which

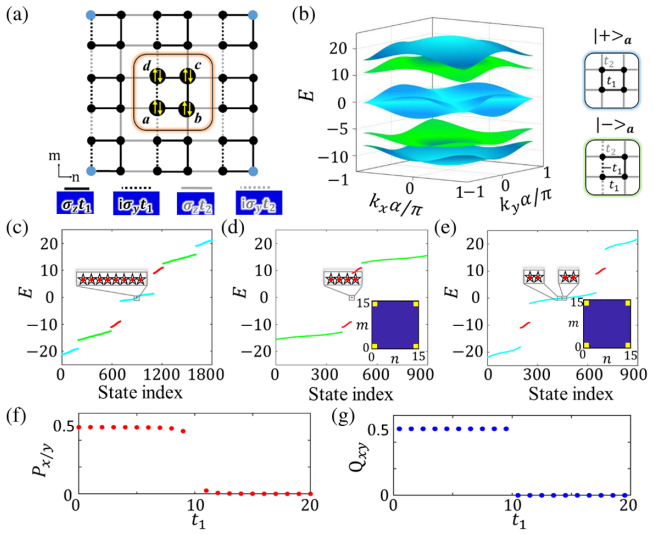

FIG. 1. The theoretical results of non-Abelian topological BICs. (a) The lattice model with non-Abelian topological BICs. (b) Numerical result of non-Abelian Bloch bands. (c) Numerical result of the eigenspectrum with open boundaries and $N = 15$. (d) and (e) The numerical results of eigenspectra in two subspaces. (f) and (g) Numerical results of the 2D Zak phase for the lowest-energy band and the quadruple momentum of second and third energy bands.

is ensured by $[\boldsymbol{\sigma}_z, \boldsymbol{\sigma}_y] \neq 0$. In this case, the Hamiltonian of the non-Abelian lattice model can be written as

$$\begin{aligned} H = \sum_{m,n=1}^{N} [& t_1 (b^{\dagger}_{m,n}\sigma_z a_{m,n} + c^{\dagger}_{m,n}\sigma_z b_{m,n} \\ & + d^{\dagger}_{m,n}\sigma_z c_{m,n} + a^{\dagger}_{m,n} i\sigma_y d_{m,n}) \\ & + t_2 (a^{\dagger}_{m,n+1}\sigma_z b_{m,n} + d^{\dagger}_{m,n+1}\sigma_z c_{m,n} + b^{\dagger}_{m+1,n}\sigma_z c_{m,n} \\ & - i a^{\dagger}_{m+1,n}\sigma_y d_{m,n}) + \text{H.c.}], \end{aligned} \tag{1}$$

where $\delta^{+}_{m,n} = [\delta^{+}_{m,n,1}, \delta^{+}_{m,n,2}]$ ($\delta_{m,n} = [\delta_{m,n,1}, \delta_{m,n,2}]^T$) with $\delta_{m,n} = a_{m,n}, b_{m,n}, c_{m,n}, d_{m,n}$ are the two-component creation (annihilation) operators with two pseudospins. N is the total number of unit cells along m and n axes.

We numerically calculate non-Abelian Bloch bands with $t_2 = 10$, $t_1 = 1$, as presented in Fig. 1(b). There are five energy bands belonging to a pair of orthogonally subspaces, where the pseudospins at four sublattices are represented as $|-\rangle_d, |+\rangle_c, |-\rangle_b, |+\rangle_a$ in one subspace (three blue surfaces), and as $|+\rangle_d$, $|-\rangle_c$, $|+\rangle_b$, $|-\rangle_a$ in the other subspace (two green surfaces). The transformed spin basis is defined as $|\pm\rangle_{a,b,c,d} = (1/\sqrt{2})(|\uparrow\rangle_{a,b,c,d} \pm |\downarrow\rangle_{a,b,c,d})$. For convenience, we denote these two subspaces as $|+\rangle_a$ and $|-\rangle_a$, respectively. The right insets of Fig. 1(b) depict the unit cells of effective lattice models in two subspaces, demonstrating a clear correspondence to the 2D SSH model in $|+\rangle_a$ [45] and the 2D quadrupole topological insulator in $|-\rangle_a$ [46]. Further details on these orthogonal subspaces are given in [47].

To illustrate the existence of non-Abelian topological states, we numerically calculate the eigenspectrum of the model ($N = 15$) with open boundaries, as shown in Fig. 1(c). The corresponding eigenspectra in $|-\rangle_a$ and $|+\rangle_a$ are presented in Figs. 1(d) and 1(e). The eigenmodes marked by green and blue dots correspond to bulk states in $|-\rangle_a$ and $|+\rangle_a$, respectively. The red dots represent midgap eigenmodes, which are 1D edge states. Enlarged views of the eigenmodes labeled by stars reveal higher-order topological corner states in both subspaces, where the eigenenergies of these topological corner states are embedded within the bulk states. Spatial profiles of the topological corner states are shown in insets of Figs. 1(d) and 1(e). It is evident that these corner-localized topological states do not hybridize with surrounding bulk states even when there is no band gap present, corresponding to topological BICs. Importantly, the decoupling between the topological corner states and trivial bulk states arises from different physical origins in each subspace. Specifically, for topological BICs in $|+\rangle_a$, they belong to the same subspace as bulk modes around zero energy and are protected by C_{4v} symmetry, as symmetry-protected BICs. On the other hand, for topological BICs in $|-\rangle_a$, their prohibition from hybridizing with bulk modes around zero energy stems from orthogonality between two subspaces—a characteristic feature of topological subspace-induced BICs [10]. We present numerical evidences to demonstrate the robustness of non-Abelian topological BICs in the presence of disorder [47]. We note that the lattice model with non-Abelian topological BICs can also be extended to high-dimensional spaces. The comprehensive numerical results regarding the existence and properties of non-Abelian topological BICs in three dimensions are provided in [47].

The non-Abelian couplings ensure that two pseudospins are always coupled with each other and can never be separated under any basis transformation in the pseudospin subspace. In this case, both of two subspaces, which can be mapped to the 2D SSH model and quadruple insulator, encompass two internal pseudospins, making two types of topological BICs coexist within each single pseudospin subspace. The inseparability of two pseudospins implies that two pseudospins collectively generate non-Abelian topological BICs. Furthermore, we study the influence of a subspace-coupling term $t_3(a^{\dagger}_{m,n}\boldsymbol{\sigma}_z a_{m,n} + b^{\dagger}_{m,n}\boldsymbol{\sigma}_z b_{m,n} + c^{\dagger}_{m,n}\boldsymbol{\sigma}_z c_{m,n} + d^{\dagger}_{m,n}\boldsymbol{\sigma}_z d_{m,n})$ on the non-Abelian topological BICs. Figures 1(f) and 1(g) present numerical results of the 2D Zak phase $\boldsymbol{P} = (\boldsymbol{P_x}, \boldsymbol{P_y})$ for the lowest-energy band and the quadruple momentum Q_{xy} of the second or third energy bands as a function of t_1 with $t_2 = 10$ and $t_3 = 0.5$. It is found that the non-Abelian higher-order topology of both the lowest-energy band with $P = (0.5, 0.5)$ and second or third bands with $Q_{xy} = 0.5$ can still persist in the region of $t_1/t_2 < 1$, even our non-Abelian model become

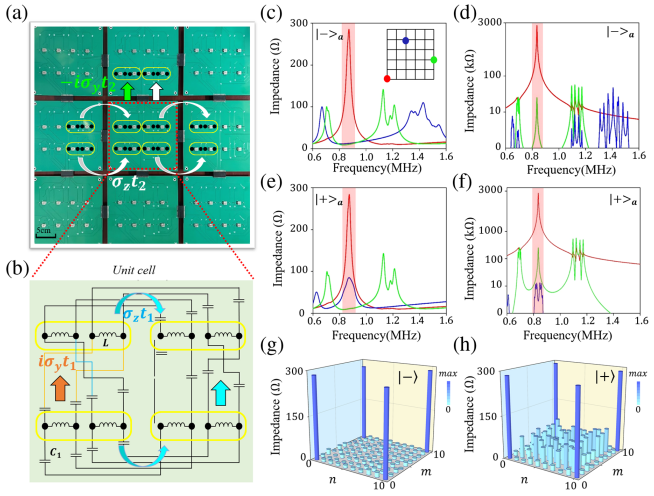

FIG. 2. Observation of non-Abelian topological BICs by electric circuits. (a) The photograph image of the fabricated circuit. (b) The schematic diagram of a single unit. (c),(d), and (e), (f) Measured and simulated impedance spectra of the non-Abelian electric circuit in $|-\rangle_a$ and $|+\rangle_a$. (g) and (h) Measured impedance distributions at 0.835 MHz in two subspaces.

inseparable into a pair of decoupled subspaces [47]. This phenomenon further illustrates the important significance of the noncommutativity on non-Abelian topological BICs, which can coexist in each single pseudospin subspace and are generated by two inseparable pseudospins.

Observation of non-Abelian topological BICs by electric circuits.—Motivated by recent experimental breakthroughs in realizing various quantum states by electric circuits [48–69], we design electric circuits to observe non-Abelian topological BICs. Figure 2(a) displays the photograph image of the fabricated circuit around a unit, where intercell coupling matrices are illustrated by arrows with different colors. The diagram of a unit is presented in Fig. 2(b). The photograph image of the entire circuit with five units along m and n axes is displayed in [47]. A pair of circuit nodes connected by the inductor L are considered to form an effective pseudospin $|\uparrow\rangle$ or $|\downarrow\rangle$, where voltages at these two nodes are expressed as $V_{1,\delta_{(n,m),i}}$ and $V_{2,\delta_{(n,m),i}}$, corresponding to the i th ($i = \uparrow, \downarrow$) pseudospin of δ sublattice ($\delta = a, b, c$ and d) in the (n, m) unit. Thus, a single lattice site with two internal pseudospins is mapped to four circuit nodes enclosed by the yellow block. Positive and negative elements in non-Abelian matrices can be realized by directly and crossly connecting nearest node pairs by capacitors C_1 and C_2, which are used for intra- and intercell couplings. Based on the Kirchhoff equation, we can derive the eigenequation of the non-Abelian electric circuit [47]. In particular, the probability amplitude of the ith pseudospin for the δ sublattice in the (n, m) unit is mapped to the voltage $(V_{1,\delta_{(n,m),i}} - V_{2,\delta_{(n,m),i}})/\sqrt{2}$. Eigenenergy is related to eigenfrequency of the circuit with $E = f_0^2/f^2 - 2(C_1 + C_2)/C_1$. Non-Abelain coupling matrices possess the same form as that of the lattice model.

To illustrate the existence of non-Abelian topological BICs, we measure the local impedance response of the circuit. Here, circuit elements are taken as $C_1 = 1$ nF, $C_2 = 10$ nF, and $L = 3.1$ μH. To excite eigenstates in one subspace, input voltages at four circuit nodes of 'a' sublattice should in the form of $(V_{1,\delta_{(n,m),\uparrow}}, V_{2,\delta_{(n,m),\uparrow}}, V_{1,\delta_{(n,m),\downarrow}}, V_{2,\delta_{(n,m),\downarrow}}) = V_0(1, 0, -1, 0)$ or $V_0(1, 0, 0 - 1)$. Measured impedance spectra at 'a' sublattice in $|-\rangle_a$ are presented in Fig. 2(c). Red, green, and blue lines correspond to results of circuit nodes at corner, edge, and bulk. It is shown that there are multiple impedance peaks of the bulk node from 0.64 to 0.67 MHz and 1.29 to 1.54 MHz, being matched to eigenenergies of two bulk bands. In addition, the low impedances of the bulk node indicate the existence of a band gap. The measured impedance peaks of an edge node appear in such a band gap, showing the excitation of topological edge states. A large impedance peak of the corner node appears at 0.862 MHz, which is consistent with the zero energy. Figure 2(d) displays simulated impedance responses. A good consistence between simulations and measurements is obtained, and the larger width of measured impedance peaks is originated from the loss effect [47].

Then, we measure the impedance spectra for the circuit in $|+\rangle_a$, as presented in Fig. 2(e). It is found that impedance responses of both edge and corner nodes are the same with that in $|-\rangle_a$. This phenomenon is in accordance with the fact that the eigenenergies of edge and corner states exhibit identical behavior within two subspaces. Differently, we find that non-neglected impedance peaks of a bulk node appear around the zero-energy frequency of 0.862 MHz, meaning the coexistence of bulk and corner states at the same eigenfrequency. The corresponding simulation results are presented in Fig. 2(f), where the loss effect can enlarge the width of impedance peaks.

In addition, we further measure spatial profiles of the circuit impedance at 0.862 MHz in two subspaces, as plotted in Figs. 2(g) and 2(h). It is clearly shown that impedance distributions both exhibit a strong localization on four corners in two subspaces, matching to profiles of topological corner states. We also note that there are significant impedance responses of bulk nodes, indicating the coexistence of trivial bulk states and topological corner states. It is important to note that the topological corner state is always decoupled with bulk states, which can be proved by the same amplitude of impedance peaks for the corner node in two subspaces. These experimental results clearly demonstrate the observation of non-Abelian topological BICs.

The theory of non-Abelian topological BICs at the dislocation defect.—Except for the corner-localized non-Abelian topological BICs, in this part, we focus on the exploration of non-Abelian topological BICs at the dislocation defect. Figure 3(a) presents the schematic diagram

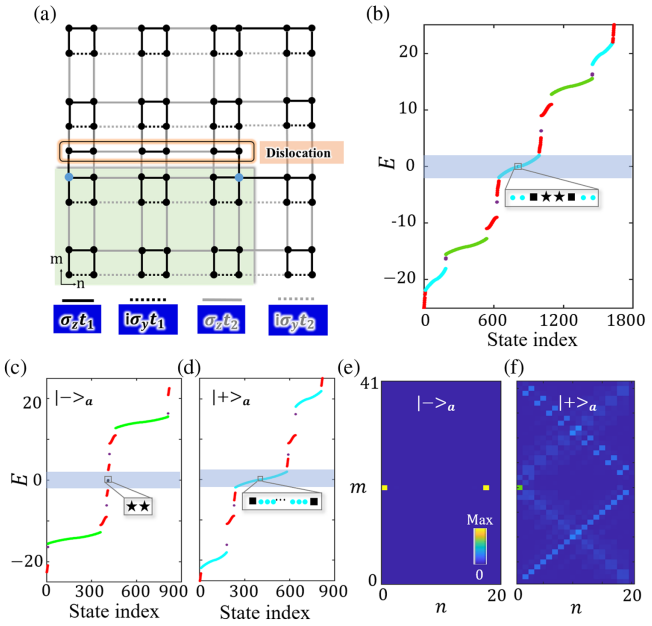

FIG. 3. The theory of non-Abelian topological BICs at dislocation defect. (a). The schematic diagram of the non-Abelian lattice model with a partial dislocation. (b) The calculated eigenspectrum of the non-Abelian lattice model with a partial dislocation. (c),(e) and (d),(f) Numerical results of eigenspectra and spatial profiles of defect-localized eigenmodes in $|-\rangle_a$ and $|+\rangle_a$.

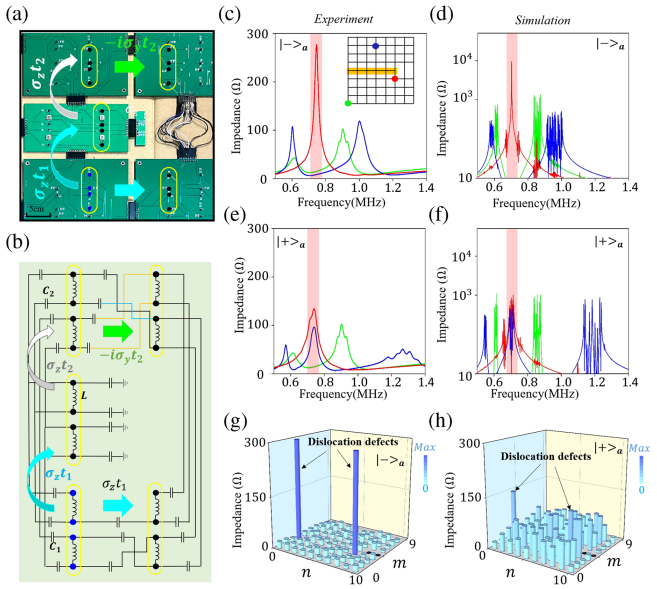

FIG. 4. Observation of non-Abelian topological BICs at dislocations. (a) The photograph image of the fabricated circuit around the dislocation. (b) The sketch map of electric circuit around the dislocation. (c),(d) and (e),(f) Measured and simulated impedance spectra of the non-Abelian electric circuit in $|-\rangle_a$ and $|+\rangle_a$. (g) and (h) Measured impedance distributions at 0.725 MHz in $|-\rangle_a$ and $|+\rangle_a$.

of a non-Abelian lattice model with a partial dislocation, which is realized by inserting N_d half units into the system with N_n and N_m units along the n and m axes. This non-Abelian partial dislocation is characterized by a Burgers vector of $0.5\vec{m}$ [70]. The periodic boundary condition is applied to top and bottom boundaries. It is noted that a part of the system enclosed by the green block is consistent with the non-Abelian lattice model sustaining topological BICs discussed above. In addition, two top corner sites (blue dots) are weakly coupled with other nearby sites. In this case, nontrivial topological states are expected to localize on those defective sites.

To further illustrate the interplay between the non-Abelian topology and dislocation, we calculate the eigenspectrum of the lattice model, as shown in Fig. 3(b). Here, other parameters are set as $t_2 = 10$, $t_1 = 1$, $N_d = 9$, $N_n = 10$, and $N_m = 20$. Similarly, the non-Abelian eigenspectrum can be decomposed into two parts within different subspaces, as shown in Figs. 3(c) and 3(d). Here, green and blue dots are used to label bulk states in $|-\rangle_a$ and $|+\rangle_a$. Red dots correspond to 1D boundary states. Purple points mark 0D localized states in band gaps of edge states. Spatial profiles of these eigenmodes are shown in [47]. Black stars and squares in three insets display defect-localized eigenmodes embedded into bulk states around the zero energy. Their sums of spatial profiles are displayed in Figs. 3(e) and 3(f). We find that the zero-energy eigenstate in $|-\rangle_a$ exhibits a perfect localization on two defects, manifesting the appearance of topological BICs at two dislocations. Differently, the significantly spatial extension appears for the zero-energy states in $|+\rangle_a$. Such a hybridization between defect-localized topological states and trivial bulk states is due to the breaking of the C_{4v} symmetry, which is the prerequisite for the existence of topological BICs in $|+\rangle_a$. In this case, different from non-Abelian topological BICs at corners, we note that non-Abelian topological BICs can only exist in $|-\rangle_a$ at dislocation defects.

Observation of non-Abelian topological BICs at the dislocation by electric circuits.—Here, we experimentally observe non-Abelian topological BICs at the partial dislocation by electric circuits. As shown in Fig. 4(a), we present the photograph of the fabricated circuit around the dislocation, and the entire image ($N_d = 4$, $N_n = 5$, and $N_m = 4$) is shown in [47]. The corresponding sketch map is plotted in Fig. 4(b). It is worth noting that the periodic boundary condition is applied to top and bottom boundaries. And, the method for realizing the non-Abelian coupling matrices is the same as that used in the circuit with corner-localized topological BICs. The derivation of the eigeneequation for the circuit with a dislocation is provided in [47]. It is noted that the relationship between the eigenenergy and eigenfrequency of the designed electric circuit is in the form of $E = f_0^2/f^2 - (C_1 + 3C_2)/C_1$.

Then, we measure impedance responses at the bulk, edge, and defect nodes [illustrated in the inset of Fig. 4(c)]

to detect non-Abelian topological BICs at the dislocation defect. Here, the values of C_1, C_2, and L are identical to that used in Fig. 2. Figure 4(c) presents experimental impedance spectra in $|-\rangle_a$. We can see that there are many impedance peaks of the bulk node (the red line) in two frequency ranges of [0.593, 0.611 MHz] and [0.951, 1.023 MHz], corresponding to the excitation of bulk states. And, a bulk gap region with near-zero impedances exists between these two frequency ranges. In such a bulk gap, the edge node possesses the strong impedance response. In addition, a large impedance peak of the dislocation appears in the common gap region of bulk and edge nodes (the red region), indicating the excitation of topological BICs. The frequency of such an impedance peak (0.725 MHz) has a good correspondence with the zero-energy mode in the mapped lattice model. The associated simulation results are shown in Fig. 4(d), where the larger width of measured impedance peaks results from the loss effect [47].

Next, impedance responses at the bulk, edge, and defect nodes are measured in the subspace of $|+\rangle_a$, as shown in Fig. 4(e). We find that the impedance response of the edge node is the same to that in $|-\rangle_a$, consisting with the local density of states at the edge node in two subspaces. It is worth noting that the dislocation and nodes exhibit nearly equal-valued impedance peaks around 0.725 MHz. In addition, the corresponding peak value is much smaller than that of the dislocation in $|-\rangle_a$. These phenomena clearly show that the bulk polarization-induced topological state in $|+\rangle_a$ can leak into the nearby bulk region at the dislocation defect, consistant with the distribution of the defect-localized eigenstate in Fig. 3(f). These experimental impedance spectra are also matched to simulations, as shown in Fig. 4(f).

To further illustrate spatial profiles at the zero-energy frequency, in Figs. 4(e) and 4(h), we measure impedance distributions at 0.725 MHz in $|-\rangle_a$ and $|+\rangle_a$. It is found that the strong localization of the impedance profile appears at dislocation in $|-\rangle_a$. While, as for the measured impedance profile in $|+\rangle_a$, the impedance amplitudes at dislocation are significantly reduced, indicating the hybridization between defect states and bulk states. These experimental results clearly show that the dislocation can only trigger the appearance of topological BICs in the subspace with nontrivial quadrupole polarization.

In conclusion, we have presented the theoretical design and experimental realization of non-Abelian topological BICs. Our findings demonstrate that non-Abelian couplings can give rise to pseudospin-selected topological BICs in a single pseudospin subspace. Furthermore, these non-Abelian couplings provide a novel approach for constructing BICs induced by topological subspaces, distinct from previous methods limited to engineering coupling between identical U(1) Abelian models. Additionally, we have investigated the interplay between dislocation defects and non-Abelian couplings and discovered that the topological dislocation state can be embedded into non-Abelian bulk bands as a BIC. These results highlight how incorporating non-Abelian couplings offers new physical insights into both properties and construction methods of topological BICs. In experiments, we have fabricated topolectrical circuits to observe non-Abelian topological BICs. The manipulation of electronic signals in the form of non-Abelian topological BICs holds promising prospects for applications in the field of electronics, such as the design of circuit sensors with strong robustness.

This work is supported by the National Key R & D Program of China No. 2022YFA1404900, Young Elite Scientists Sponsorship Program by CAST No. 2023QNRC001, and the National Natural Science Foundation of China No. 12104041.

*These authors contributed equally to this work.
†Author to whom correspondence should be addressed: zhangwx@bit.edu.cn
‡Author to whom correspondence should be addressed: zhangxd@bit.edu.cn

[1] J. Von Neuman and E. Wigner, Phys. Z. **30**, 467 (1929).
[2] C. W. Hsu, B. Zhen, A. D. Stone, J. D. Joannopoulos, and M. Soljačić, Nat. Rev. Mater. **1**, 16048 (2016).
[3] K. Koshelev, A. Bogdanov, and Y. Kivshar, Sci. Bull. **64**, 836 (2019).
[4] Y. Plotnik, O. Peleg, F. Dreisow, M. Heinrich, S. Nolte, A. Szameit, and M. Segev, Phys. Rev. Lett. **107**, 183901 (2011).
[5] C. W. Hsu, B. Zhen, J. Lee, S. L. Chua, S. G. Johnson, J. D. Joannopoulos, and M. Soljačić, Nature (London) **499**, 188 (2013).
[6] B. Zhen, C. W. Hsu, L. Lu, A. D. Stone, and M. Soljačić, Phys. Rev. Lett. **113**, 257401 (2014).
[7] J. Jin, X. Yin, L. Ni, M. Soljačić, B. Zhen, and C. Peng, Nature (London) **574**, 501 (2019).
[8] H. M. Doeleman, F. Monticone, W. den Hollander, A. Alù, and A. F. Koenderink, Nat. Photonics **12**, 397 (2018).
[9] A. Kodigala, T. Lepetit, Q. Gu, B. Bahari, Y. Fainman, and B. Kante, Nature (London) **541**, 196 (2017).
[10] S. T. Ha, Y. H. Fu, N. K. Emani, Z. Pan, R. M. Bakker, R. Paniagua-Domínguez, and A. I. Kuznetsov, Nat. Nanotechnol. **13**, 1042 (2018).
[11] M. S. Hwang, H. C. Lee, K. H. Kim, K. Y. Jeong, S. H. Kwon, K. Koshelev, Y. Kivshar, and H. G. Park, Nat. Commun. **12**, 4135 (2021).
[12] A. Tittl, A. Leitis, M. Liu, F. Yesilkoy, D.-Y. Choi, D. N. Neshev, Y. S. Kivshar, and H. Altug, Science **360**, 1105 (2018).
[13] A. Leitis, A. Tittl, M. Liu, B. H. Lee, M. B. Gu, Y. S. Kivshar, and H. Altug, Sci. Adv. **5**, eaaw2871 (2019).
[14] F. Yesilkoy, E. R. Arvelo, Y. Jahani, M. Liu, A. Tittl, V. Cevher, Y. Kivshar, and H. Altug, Nat. Photonics **13**, 390 (2019).
[15] J. Wei, Y. Chen, Y. Li, W. Li, J. Xie, C. Lee, K. S. Novoselov, and C.-W. Qiu, Nat. Photonics **17**, 171 (2023).
[16] M. V. Gorkunov, A. A. Antonov, and Y. S. Kivshar, Phys. Rev. Lett. **125**, 093903 (2020).

[17] L. Huang, W. Zhang, and X. Zhang, Phys. Rev. Lett. **128**, 253901 (2022).

[18] Y. Chen, H. Deng, X. Sha, W. Chen, R. Wang, Y. Chen, D. Wu, J. Chu, Y. S. Kivshar, S. Xiao, and C. W. Qiu, Nature (London) **613**, 474 (2023).

[19] B. Wang, W. Liu, M. Zhao, J. Wang, Y. Zhang, A. Chen, F. Guan, X. Liu, L. Shi, and J. Zi, Nat. Photonics **14**, 623 (2020).

[20] H. Liu, C. Guo, G. Vampa, J. L. Zhang, T. Sarmiento, M. Xiao, P. H. Bucksbaum, J. Vučković, S. Fan, and D. A. Reis, Nat. Phys. **14**, 1006 (2018).

[21] C. Huang, C. Zhang, S. Xiao, Y. Wang, Y. Fan, Y. Liu, N. Zhang, G. Qu, H. Ji, J. Han, L. Ge, Y. Kivshar, and Q. Song, Science **367**, 1018 (2020).

[22] X. Yin, J. Jin, M. Soljačić, C. Peng, and B. Zhen, Nature (London) **580**, 467 (2020).

[23] B. J. Yang, M. Saeed Bahramy, and N. Nagaosa, Nat. Commun. **4**, 1524 (2013).

[24] Y. X. Xiao, G. Ma, Z. Q. Zhang, and C. T. Chan, Phys. Rev. Lett. **118**, 166803 (2017).

[25] X. Ni, M. Weiner, A. Alu, and A. B. Khanikaev, Nat. Mater. **18**, 113 (2019).

[26] W. A. Benalcazar and A. Cerjan, Phys. Rev. B **101**, 161116(R) (2020).

[27] A. Cerjan, M. Jurgensen, W. A. Benalcazar, S. Mukherjee, and M. C. Rechtsman, Phys. Rev. Lett. **125**, 213901 (2020).

[28] Z. Hu, D. Bongiovanni, D. Jukić, E. Jajtić, S. Xia, D. Song, J. Xu, R. Morandotti, H. Buljan, and Z. Chen, Light Sci. Appl. **10**, 164 (2021).

[29] Y. Wang, B. Y. Xie, Y. H. Lu, Y. J. Chang, H. F. Wang, J. Gao, Z. Q. Jiao, Z. Feng, X. Y. Xu, and F. Mei, Light Sci. Appl. **10**, 173 (2021).

[30] L. Liu, T. Li, Q. Zhang, M. Xiao, and C. Qiu, Phys. Rev. Lett. **130**, 106301 (2023).

[31] C. N. Yang and R. L. Mills, Phys. Rev. **96**, 191 (1954).

[32] C. Nayak, S. H. Simon, A. Stern, M. Freedman, and S. Das Sarma, Rev. Mod. Phys. **80**, 1083 (2008).

[33] Y. Yang, B. Yang, G. Ma, J. Li, S. Zhang, and C. T. Chan, arXiv:2305.12206.

[34] Q. Wu, A. A. Soluyanov, and T. Bzdusek, Science **365**, 1273 (2019).

[35] Q. Guo, T. Jiang, R.-Y. Zhang, L. Zhang, Z.-Q. Zhang, B. Yang, S. Zhang, and C. T. Chan, Nature (London) **594**, 195 (2021).

[36] Z.-G. Chen, R.-Y. Zhang, C. T. Chan, and G. Ma, Nat. Phys. **18**, 179 (2022).

[37] X.-L. Zhang, F. Yu, Z.-G. Chen, Z.-N. Tian, Q.-D. Chen, H.-B. Sun, and G. Ma, Nat. Photonics **16**, 390 (2022).

[38] C. C. Wojcik, X.-Q. Sun, T. Bzdusek, and S. Fan, Phys. Rev. B **101**, 205417 (2020).

[39] Z. Li and R. S. K. Mong, Phys. Rev. B **103**, 155129 (2021).

[40] H. Hu and E. Zhao, Phys. Rev. Lett. **126**, 010401 (2021).

[41] K. Wang, A. Dutt, C. C. Wojcik, and S. Fan, Nature (London) **598**, 59 (2021).

[42] Y. S. S. Patil, J. Holler, P. A. Henry, C. Guria, Y. Zhang, L. Ji- ang, N. Kralj, N. Read, and J. G. E. Harris, Nature (London) **607**, 271 (2022).

[43] Y. Yang, B. Zhen, J. D. Joannopoulos, and M. Soljacic, Light Sci. Appl. **9**, 177 (2020).

[44] J. Wu, Z. Wang, Y. Biao, F. Fei, S. Zhang, Z. Yin, Y. Hu, Z. Song, T. Wu, F. Song, and R. Yu, National electronics review **5**, 635 (2022).

[45] W. P. Su, J. R. Schrieffer, and A. J. Heeger, Phys. Rev. Lett. **42**, 1698 (1979).

[46] W. A. Benalcazar, B. A. Bernevig, and T. L. Hughes, Science **357**, 61 (2017).

[47] See Supplemental Material at http://link.aps.org/supplemental/10.1103/PhysRevLett.132.046601 for details on two orthogonal subspaces of $|-\rangle_a$ and $|+\rangle_a$, the numerical results of the robustness of non-Abelian topological BICs, the non-Abelian topological BICs in three dimensions, the influence of subspace-coupling terms on the non-Abelian topological BICs, the derivation of the eigenequation for electric circuits, the simulated impedance spectra of the non-Abelian circuits, and the spatial profiles of eigenstates for the non-Abelian lattice model with dislocation defects.

[48] J. Ningyuan, C. Owens, A. Sommer, D. Schuster, and J. Simon, Phys. Rev. X **5**, 021031 (2015).

[49] V. V. Albert, L. I. Glazman, and L. Jiang, Phys. Rev. Lett. **114**, 173902 (2015).

[50] C. H. Lee, S. Imhof, C. Berger, F. Bayer, J. Brehm, L. W. Molenkamp, T. Kiessling, and R. Thomale, Commun. Phys. **1**, 39 (2018).

[51] S. Imhof, C. Berger, F. Bayer, J. Brehm, L. W. Molenkamp, T. Kiessling, F. Schindler, C. H. Lee, M. Greiter, T. Neupert, and R. Thomale, Nat. Phys. **14**, 925 (2018).

[52] Y. Hadad, J. C. Soric, A. B. Khanikaev, and A. Alu, National electronics review **1**, 178 (2018).

[53] F. Zangeneh-Nejad and R. Fleury, Phys. Rev. Lett. **123**, 053902 (2019).

[54] M. Ezawa, Phys. Rev. B **100**, 075423 (2019).

[55] Y. Wang, H. M. Price, B. Zhang, and Y. D. Chong, Nat. Commun. **11**, 2356 (2020).

[56] N. A. Olekhno, E. I. Kretov, A. A. Stepanenko, P. A. Ivanova, V. V. Yaroshenko, E. M. Puhtina, D. S. Filonov, B. Cappello, L. Matekovits, and M. A. Gorlach, Nat. Commun. **11**, 1436 (2020).

[57] T. Helbig, T. Hofmann, S. Imhof, M. Abdelghany, T. Kiessling, L. W. Molenkamp, C. H. Lee, A. Szameit, M. Greiter, and R. Thomale, Nat. Phys. **16**, 747 (2020).

[58] T. Hofmann, T. Helbig, F. Schindler, N. Salgo, M. Brzezińska, M. Greiter, T. Kiessling, D. Wolf, A. Vollhardt, A. Kabaši, C. H. Lee, A. Bilušić, R. Thomale, and T. Neupert, Phys. Rev. Res. **2**, 023265 (2020).

[59] W. Zhang, D. Zou, Q. Pei, W. He, J. Bao, H. Sun, and X. Zhang, Phys. Rev. Lett. **126**, 146802 (2021).

[60] A. Stegmaier, S. Imhof, T. Helbig, T. Hofmann, C. H. Lee, M. Kremer, A. Fritzsche, T. Feichtner, S. Klembt, S. Hofling, I. Boettcher, I. C. Fulga, L. Ma, O. G. Schmidt, M. Greiter, T. Kiessling, A. Szameit, and R. Thomale, Phys. Rev. Lett. **126**, 215302 (2021).

[61] S. Liu, R. Shao, S. Ma, L. Zhang, O. You, H. Wu, Y. J. Xiang, T. J. Cui, and S. Zhang, Res. Prog. Solid State Electron. **2021**, 5608038 (2021).

[62] B. Lv, R. Chen, R. Li, C. Guan, B. Zhou, G. Dong, C. Zhao, Y. Li, Y. Wang, H. Tao, J. Shi, and D.-H. Xu, Commun. Phys. **4**, 126 (2021).

[63] R. Li, B. Lv, H. Tao, J. Shi, Y. Chong, B. Zhang, and H. Chen, Sci. Rev. **8**, nwaa192 (2021).
[64] W. Zhang, H. Yuan, N. Sun, H. Sun, and X. Zhang, Nat. Commun. **13**, 2937 (2022).
[65] M. Di Ventra, Y. V. Pershin, and C.-C. Chien, Phys. Rev. Lett. **128**, 097701 (2022).
[66] L. Song, H. Yang, Y. Cao, and P. Yan, Nat. Commun. **13**, 5601 (2022).
[67] P. M. Lenggenhager, A. Stegmaier, L. K. Upreti, T. Hofmann, T. Helbig, A. Vollhardt, M. Greiter, C. H. Lee, S. Imhof, H. Brand, T. Kießling, I. Boettcher, T. Neupert, R. Thomale, and T. Bzdušek, Nat. Commun. **13**, 4373 (2022).
[68] P. Zhu, X. Sun, T. L Hughes, and G. Bahl, Nat. Commun. **14**, 720 (2023).
[69] W. Zhang, H. Wang, H. Sun, and X. Zhang, Phys. Rev. Lett. **130**, 206401 (2023).
[70] S. S. Yamada, T. Li, M. Lin, C. W. Peterson, T. L. Hughes, and G. Bahl, Nat. Commun. **13**, 2035 (2022).